shows that the basic processes of floral organ specification are evolutionarily old, and that the very different forms taken by flowers of different plant families, at least among the dicotyledonous plants, result from more recent modifications of developmental processes. This recognition allows experimental approaches to morphological evolution as wild-type or altered *Antirrhinum* genes can now be introduced into *Arabidopsis* plants with mutations in the homologous gene. When *Antirrhinum* transformation procedures are discovered, the converse experiment will also be possible. Such experiments will reveal whether the evolutionary changes that lead to the very different flower forms of the two plants are due to changes in the homeotic genes themselves, changes in their regulators, or changes in the downstream genes that they regulate.

The second conclusion is that the processes of flower development that have been revealed are remarkably size-invariant. *Arabidopsis thaliana* flowers, when mature, have a mass of around 550 µg, whereas *Antirrhinum majus* flowers have a mass more than 1,000 times greater. Nonetheless, the basic processes that specify their meristem and organ types appear to be homologous. We soon may learn how the relative timing of cell division and regulatory gene expression are controlled, and how the domains of gene expression are developmentally regulated, and thus comprehend how similar structures of very different sizes may evolve from a common ancestor. ☐

Enrico S. Coen is at the Department of Genetics, John Innes Institute, Colney Lane, Norwich NR4 7UH, UK; Elliot M. Meyerowitz is at the Division of Biology, California Institute of Technology, Pasadena, California 91125, USA.

1. Pruitt, R. E., Chang, C., Pang, P.P.-Y. & Meyerowitz, E.M. in *Genetic Regulation of Development* (ed. W. R. Loomis) 327–338 (Liss, New York, 1987).
2. Bowman, J. L., Yanofsky, M. F. & Meyerowitz, E. M. *Oxford Surv. Plant molec cell. Biol.* **5**, 57–87 (1988).
3. Haughn, G. W. & Somerville, C. R. *Devl Genet.* **9**, 73–89 (1988).
4. Komaki, M. K., Okada, K., Nishino, E. & Shimura, Y. *Development* **104**, 195–203 (1988).
5. Bowman, J. L., Smyth, D. R. & Meyerowitz, E. M. *Pl. Cell* **1**, 37–52 (1989).
6. Meyerowitz, E. M., Smyth, D. R. & Bowman, J. L. *Development* **106**, 209–217 (1989).
7. Kunst, L., Klenz, J. E., Martinez-Zapater, J. & Haughn, G. W. *Pl. Cell* **1**, 1195–1208 (1989).
8. Carpenter, R. & Coen, E. S. *Genes Dev.* **4**, 1483–1493 (1990).
9. Schwarz-Sommer, Z., Huijser, P., Nacken, W., Saedler, H. & Sommer, H. *Science* **250**, 931–936 (1990).
10. Bowman, J. L., Smyth, D. R. & Meyerowitz, E. M. *Development* **112**, 1–20 (1991).
11. Coen, E. S. *A. Rev. Pl. Physiol. Pl. molec. Biol.* **42**, 241–279 (1991).
12. Meyerowitz, E. M. *et al. Development* **112** suppl. 1, 157–168 (1991).
13. Sommer, H. *et al. EMBO J.* **9**, 605–613 (1990).
14. Yanofsky, M. F. *et al. Nature* **346**, 35–39 (1990).
15. Norman, C., Runswick, M., Pollock, R. & Treisman, R. *Cell* **55**, 989–1003 (1988).
16. Boxer, L. M., Prywes, R., Roeder, R. G., & Kedes, L. *Molec. cell. Biol.* **9**, 515–522 (1989).
17. Passmore, S., Maine, G. T., Elble, R., Christ, C. & Tye, B. K. *J. molec. Biol.* **204**, 593–606 (1988).
18. Herskowitz, I. *Nature* **342**, 749–757 (1989).
19. Ma, H., Yanofsky, M. F. & Meyerowitz, E. M. *Genes Dev.* **5**, 484–495 (1991).
20. Drews, G. N., Bowman, J. L. & Meyerowitz, E. M. *Cell* **65**, 991–1002 (1991).
21. Kuckuck, H. Z. *Indukt. Abst. Vererbungsl.* **56**, 51–83 (1936).
22. Stubbe, H., *Genetik und Zytologie von Antirrhinum L. sect. Antirrhinum* (Gustav Fischer, Jena, 1966).
23. Irish, V. F. & Sussex, I. M. *Pl. Cell* **2**, 741–753 (1990).
24. Coen, E. S. *et al. Cell* **63**, 1311–1322 (1990).
25. Mermod, N., O'Neill, E. A., Kelly, T. J. & Tjian, R. *Cell* **58**, 741–753 (1989).
26. Struhl, K. *Trends biochem. Sci.* **14**, 137–140 (1989).
27. Weberling, F. *Morphology of Flowers and Inflorescences* (Cambridge University Press, Cambridge, 1989).

ARTICLES

Tomographic imaging of subducted lithosphere below northwest Pacific island arcs

Rob van der Hilst*, Robert Engdahl†, Wim Spakman‡ & Guust Nolet‡§

* Department of Earth Sciences, University of Leeds, Leeds LS2 9JT, UK
† National Earthquake Information Center, US Geological Survey, DFC, Box 25046, Stop 967, Denver, Colorado 80225, USA
‡ Department of Theoretical Geophysics, University of Utrecht, Budapestlaan 4, 3508 TA Utrecht, The Netherlands

The seismic tomography problem does not have a unique solution, and published tomographic images have been equivocal with regard to the deep structure of subducting slabs. An improved tomographic method, using a more realistic background Earth model and surface-reflected as well as direct seismic phases, shows that slabs beneath the Japan and Izu Bonin island arcs are deflected at the boundary between upper and lower mantle, whereas those beneath the northern Kuril and Mariana arcs sink into the lower mantle.

THE depth range involved in the recycling of material from the Earth's surface back into the mantle has been among the most controversial issues in geodynamics in the past two decades. Many studies have investigated the fate of subducted lithosphere near the transition between the upper and lower mantle to learn more about the amount of mass transport across this boundary[1]. Although many seismologists explain the lower-mantle heterogeneity beneath Middle America on the basis of deep subduction of the Farallon/Pacific plate[2-8], the subject has remained controversial in studies of northwest Pacific subduction zones.

In the northwest Pacific, where old lithosphere of the Pacific plate subducts below island arcs[9], Jordan and coworkers[10-13] concluded from residual sphere analyses that the subducted slab continues below the deepest earthquakes, to depths of at least 1,200 km. There is some evidence to support this interpretation[14-17]; other studies, however, have suggested that the images of subducted slabs determined by this method can be influenced by noise in the data and by effects of lower-mantle and near-receiver structure[18-22].

Variations in the propagation velocity of seismic waves owing to the presence of subducted lithosphere can be imaged by seismic tomography. The tomographic method employed in this study involves the interpretation of seismic-wave arrival-times determined from millions of seismograms in terms of the Earth's three-dimensional structure. The controversial issues concerning deep subduction have not so far been satisfactorily resolved by

§ Now at: Department of Geological and Geophysical Sciences, Princeton University, Princeton, NJ 08544, USA.

tomographic studies, mainly because of the lack of high-quality seismic data. Another problem is the strong nonlinearity of the tomographic problem, which requires linearization with respect to a background Earth model that closely mimics the real Earth. The solutions of linearized inversions are necessarily close to this *a priori* model. Published results are equivocal but mathematically acceptable as 'minimum norm solutions'[23] of the inversion, and resolution tests have been used to claim their reliability. The tests commonly used to assess the reliability of tomographic images determined by linear inversion do not, however, address the influence of the *a priori* assumptions and data quality.

Our objectives are to demonstrate that the use of different seismic data and *a priori* assumptions can easily result in different tomographic images, and that improvements in the reference Earth model and, as a consequence, in the seismic data and earthquake hypocentres routinely reported by international data centres, result in better tomographic images. Important innovations to current methods introduced in this study are the recomputation of earthquake hypocentres and the re-identification of associated P- and pP-wave data using the reference model iasp91 (ref. 24) before the inversion for three-dimensional structure.

The iasp91 model is a good description of the spherically averaged velocities of longitudinal waves below the study region, which is a requirement for a proper linearization of the inversion problem. The use of the iasp91 model and data from the direct P and surface-reflected pP waves from improved hypocentres provides information about deep slab structure that is more reliable than previous inversions based solely on P data and hypocentres reported by the International Seismological Centre (ISC). The images resulting from our improved method reveal relatively short slabs with high seismic velocity relative to surrounding mantle material. In contrast, the inversion of uncorrected ISC P-wave data resulted in long slabs, penetrating to lower-mantle depths, with smaller variations in seismic velocity. The new images indicate slab deflection at the 670-km discontinuity from southern Kuril to central Izu Bonin, but suggest mass transport to lower-mantle depths below the northern Kurile and the Mariana arcs.

Advantages of pP data

In the northwest Pacific, earthquakes and seismological stations are confined mainly to narrow zones along plate boundaries (Fig. 1). When the data set consists entirely of direct P-wave data, this distribution of earthquakes and stations causes a number of problems in the resolution of subduction-zone structure by tomographic imaging[25]. First, shallow structures below intraplate regions will not be recovered because of inadequate sampling. Second, because direct waves travel predominantly either upwards to stations along the arc or steeply downwards

to more-distant stations, and only few waves are oblique to the slab plane, 'smearing' of structure along the ray paths will occur and slab structure cannot be resolved unambiguously[26]. Third, an uneven station distribution can result in biased or poorly constrained hypocentres and loss of structurally related signal in the data.
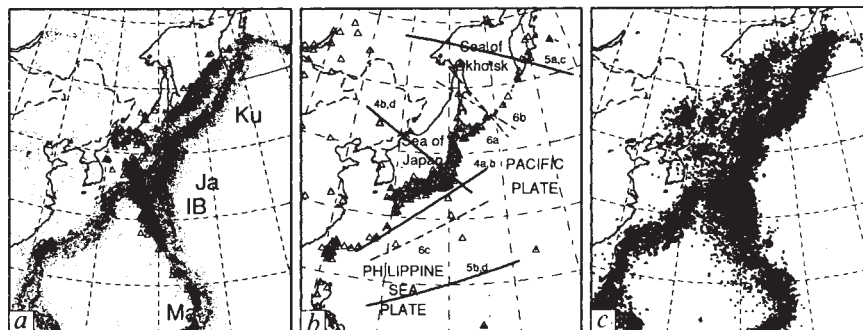
These problems are reduced by augmenting the data set used for the tomographic imaging by data from the seismic phase pP (ref. 25). This phase is a longitudinal wave that initially radiates upwards from the hypocentre, is reflected at the Earth's surface, and subsequently travels to a distant seismological station. The pP phase is sometimes called a depth phase because the phase can be observed only for earthquake hypocentres with non-zero depth. The northwest Pacific region is very suitable for the incorporation of the pP phase in tomographic imaging because of the numerous deep earthquakes and, in most cases, the substantial spatial separation between P- and pP-wave ray paths. The distribution of pP reflection points (Fig. 1c) indicates that pP-wave ray paths geometrically sample mantle structure beneath the intraplate regions more adequately than do direct P waves. Moreover, pP-wave ray paths are often oblique to ray paths of the direct P waves. This enhances the resolution along P-wave ray paths and thus counteracts the 'smearing' of velocity anomalies. In addition, the combined use of P- and pP-wave arrival times puts strong constraints on the earthquake focal depth[27,28] which limits the trade-off between uncertainties in earthquake location and variations in P-wave velocity.

In spite of these obvious advantages, the pP phase has not been used in tomographic imaging until recently because the data were suspected of being unreliable. Van der Hilst and Engdahl[25], however, investigated possible sources of error and showed that, after careful processing, pP data could significantly improve tomographic images of mantle structure beneath the Caribbean region. The statistical properties of pP data reported by the ISC for northwest Pacific earthquakes are summarized in Fig. 2a. The frequency distribution of the ISC pP data is skewed to negative values but has a large positive tail. This tail is due mainly to misidentifications of other later-arriving depth phases such as sP (initially transverse compressional wave) and water-reflected pwP, most of which can be recognized and removed before inversion (R.E. and R.v.d.H., manuscript in preparation, hereafter referred to as EH91).

Earthquake relocation

In delay-time tomography, *a priori* knowledge of seismic velocities in the Earth's interior (the reference model) is used to linearize the inversion problem[23]. This reference model is then used for estimating earthquake locations, for calculating travel times, and for computing approximate ray paths along which the seismic waves travel from source to receiver. The delay time, or travel-time residual, is the difference between the

FIG. 1 *a*, Epicentres of the northwest Pacific earthquakes used in this study (time period: 1964–1989). Two intervals of focal depth are distinguished: dots, 0–300 km ($N = 38,484$) and triangles, 300–700 km ($N = 1,753$). Abbreviations denote the Kuril (Ku), Japan (Ja), Izu Bonin (IB) and Mariana (Ma) island arcs. *b*, Locations of the seismological stations within the study region. The 323 stations contributed 544,865 travel-time residuals to the data set. We also used data from 1,961 stations outside the study region, primarily in Europe and North America, which contributed 1,363,431 P-wave data. These data are corrected for delays acquired along the P- and pP-wave ray paths outside the Earth's volume under study (see text for discussion).

The solid and dashed lines depict the strikes of the mantle cross-sections shown in Figs 4 and 5 and Fig. 6 respectively. *c*, The distribution of 83,831 pP reflection points. The reflection points are computed in a spherical Earth model. The pP data (Fig. 2c) are corrected for water depth or topography above the reflection point.

observed and calculated arrival times of a seismic wave. In most tomographic studies the Jeffreys–Bullen (JB) model for P-wave velocities[29] is used, with earthquake locations and seismic data reported by the ISC without further processing. A disadvantage of the JB model is the smoothness of the velocity–depth profile at depths where upper-mantle discontinuities are known to exist. This difference between JB and the true Earth degrades the linearization and can result in reference-model artefacts at depths of particular interest[30]. Here we use the iasp91 reference model[24], which has rapid increases in P-wave velocity at depths of 410 and 660 km.

There are also good reasons to redetermine the hypocentral parameters published by the ISC. The hypocentres used by the ISC to determine travel-time residuals are computed from P-wave arrival times only. The presence of lateral heterogeneity near the source and the peculiarities of station distribution about most subduction zones can combine to produce a depth bias[31]. Indeed, the large negative mean of reported ISC pP delay times (Fig. 2a and ref. 25) suggests that the focal depths of many subduction zone earthquakes have been overestimated and the associated pP phases potentially misidentified by the ISC (ref. 25, EH91).

For delay-time tomography this problem with ISC hypocentres has two important effects. First, the use of negative reported pP delay times can result in tomographic images that are improperly biased to higher velocities beneath pP reflection points. Second, errors in earthquake hypocentres tend to absorb structurally related signals along P-wave paths near the source, which are not fully recoverable on tomographic inversion.

Before inversion, a combination of ISC P- and pP-wave arrival times and the iasp91 velocity model were used to redetermine earthquake hypocentres in the northwest Pacific region (EH91). New travel-time residuals for reidentified P and pP phases (hereafter referred to as NWP data) were computed from the relocated hypocentres. Figs 2 and 3 demonstrate the effect of the use of iasp91 and hypocentre relocation on the distribution of P and pP residuals. The relocation with the additional information from the pP phase would also lead to reduced variance for pP data even if the JB model were retained as the background Earth model. But for reasons mentioned earlier and because of the large amounts of computer time involved in the relocation procedure, we have relocated directly using the iasp91 model. The improvement is clear from the histograms in Fig. 2.

The variance reduction for P and pP data (Figs 2 and 3) is significant with respect to variance reductions typically obtained

from tomographic inversion[26,32–34]. This demonstrates that in linearized tomographic inversions of uncorrected ISC data there is a danger of incorrectly mapping inadequacies in the reference model and errors in the earthquake hypocentres into the three-dimensional structure being determined.

Subduction-zone morphology and mantle structure

Jordan and coworkers[10-13] advocated the penetration of subducted slab to depths of at least 1,200 km below northwest Pacific island arcs. From tomographic studies with P-wave data, some investigators have supported this interpretation[16,17,34] whereas, others suggested that slab penetration occurs only locally[19,33,35]. To better understand this disagreement we compare below inversions of reported ISC P data with inversions of our NWP P and pP data (Figs 4 and 5). In our discussion we focus on the structure near the transition from upper to lower mantle.

We inverted delay times for aspherical variations in seismic velocity, for hypocentre relocation owing to near-source heterogeneity, and for station corrections. For the inversion we employed a damped least-squares method based on the LSQR algorithm[36–39]. We will present the complete results of our inversion elsewhere (R.v.d.H., R.E. & W.S., manuscript in preparation, hereafter referred to as HES91).

The inversion results obtained from reported ISC P data using a JB reference (Figs 4a, b and 5a, b) are characterized by a number of important general features. Higher-than-average P-wave velocities are imaged in upper-mantle regions where subduction of the Pacific plate is known to occur. The images suggest continuity of the high-velocity zones across the 670-km discontinuity, although the amplitude of the lower-mantle velocity variations relative to JB (~2%) are smaller than in the upper mantle (~3%). In the upper mantle, the locations of earthquakes correlate reasonably well with the regions of high P-wave velocity, although the dip of the Wadati–Benioff zone deviates locally from the dip of the imaged high-velocity zone. In the mantle above the seismic zone, amplitudes of aspherical variations of P-wave velocity are low. Locally, an increase in P-wave velocity is imaged near a depth of 670 km.

For upper-mantle regions in the vicinity of the Wadati–Benioff zones, results of tomographic inversions of NWP P and pP data using the iasp91 reference model (Figs 4c, d and 5c, d) do not differ significantly from the ISC images. In detail, however, there are differences in the amplitudes of the velocity variations, and in the correlation between seismicity and zones of high P-wave velocities. The amplitudes of the velocity perturbations
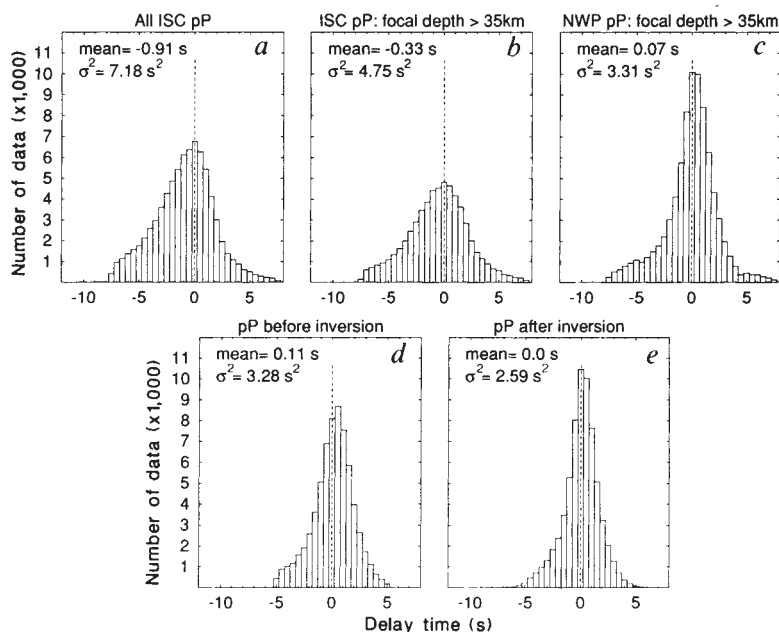
FIG. 2 Frequency distribution of pP data at different stages of data processing. a, pP data reported by the ISC between 1964 and 1987. These data are used only to identify pP data initially, but are not used in our inversions. b, The distribution of ISC pP data from earthquakes with a focal depth larger than 35 km. The maximum value of the travel-time residual is 7.5 s. c, The distribution of NWP pP delay times, which are computed (EH91) from hypocentres that are relocated in the iasp91 model for P-wave velocities[24]. The maximum value of the travel-time residual is 7.5 s. With respect to the distribution in b, a variance reduction of pP data of 30% was obtained. d, The distribution of NWP pP data after the construction of 66,042 composite rays[36] and the deletion of pP data with residuals larger than 5 s. This is the distribution of the pP data before inversion. e, The distribution of pP data after tomographic inversion. On inversion for three-dimensional mantle structure, a further variance reduction of 21% was obtained after 35 iterations of the damped LSQR inversion algorithm[36,37].

near the deepest earthquakes of the Wadata–Benioff zones are substantially higher in the NWP than in the ISC images.

Differences between the NWP and ISC images are substantial in mantle regions where aspherical Earth structure is not indicated by seismicity. The inversion of ISC P-wave data reveals a zone of moderately high P-wave velocity continuous to lower-mantle depths in all cross-sections. In contrast, our new results indicate that fast slab-like regions in the lower mantle are found only below the deepest earthquakes of the Kuril and Mariana subduction zones (Figs 5c, d and 6a). The new images suggest, however, a maximum depth of about 850 km for the high-velocity zone below the northern Kuril arc (Figs 5c and 6a), whereas no maximum depth was indicated from the inversion of ISC P-wave data (Fig. 5a). Figure 6a suggests the broadening of the Kuril slab across the transition from upper to lower mantle. The vertical mantle sections across the northern part of the Philippine Sea Plate (Figs 4c and 6c), the Sea of Japan (Fig. 4d) and the southern Kuril arc (Fig. 6b) show images of fast slab-like zones deflected at depths between 500 and 670 km. Figure 6b and c illustrates upper to lower mantle. The relationship between the images of high P-wave velocities and unusual locations of earthquakes several hundreds of kilometres off the inclined Wadati–Benioff zones[40,41]. Okino et al.[40] explained observed P-wave arrival times from an earthquake off the Izu Bonin seismic zone (Fig. 6c) by a model of a deflected slab with a P-wave propagation 3.5% faster than in the JB model. This is in good agreement with the results from our tomographic imaging (Figs 4c and 6c).

Vertical velocity contrasts at a depth of 670 km are absent in the NWP images. This was expected, as we corrected for the presence of the 670-km discontinuity by using iasp91 rather than

JB as the reference model (compare Figs 5b and d). The section across the southern Philippine Sea (Fig. 5c), however, shows a rapid increase in P-wave velocity between the 410- and 670-km discontinuities. Below the northern part of the Philippine Sea and the Sea of Japan, a comparable increase in P-wave velocity at a depth of about 500 km coincides with the upper boundary of the deflected continuations of the slab-like structures below the northern Izu Bonin, Japan and southern Kuril arcs (Figs 4c, d and 6b). These observations suggest that a seismic discontinuity at a depth near 520 km (ref. 42) is associated at least locally with subducted lithosphere deflected at the base of the upper mantle[43].

Reliability of the tomographic images

The reliability of results of large-scale inversions is assessed by calculating the response to a synthetic input model[8,33,36,44]. But these resolution tests do not reflect inadequacies of the reference model, systematic errors in the data, inconsistencies between travel times and earthquake locations and ray paths, and biases in earthquake location. As a consequence, the effect on resolution of the use of better data, earthquake locations and reference model cannot be demonstrated by resolution tests. But in regions where the sampling by P-wave ray paths only is inadequate, significant improvement in computed resolution is obtained with the additional ray-path coverage and focal-depth resolution provided by the pP-wave data (HES91). This applies in particular to mantle structure beneath intraplate regions and to deflected aseismic parts of the subducted slab. In studies in which only P-wave ray paths are used, these mantle regions are often overlooked[34] or characterized by a lack of horizontal resolution[19,26,33].
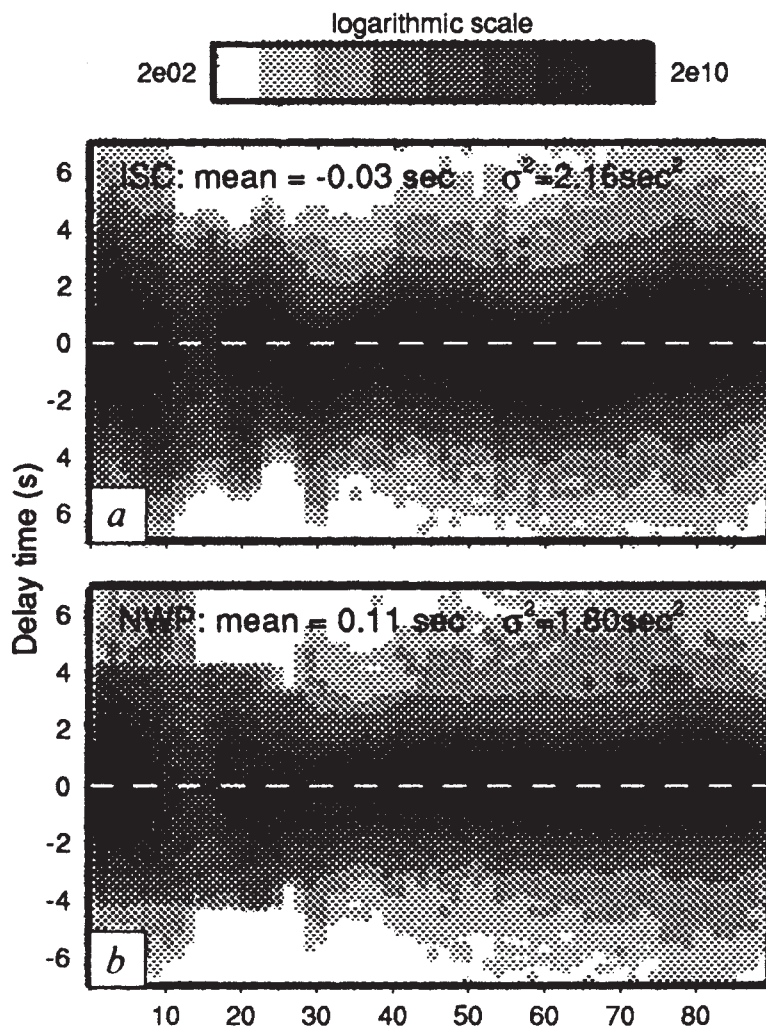
FIG. 3 The distribution of P-wave travel-time residuals versus epicentral distance. a, P delay times reported by the ISC (1964–1987) and the National Earthquake Information Center (NEIC, 1987–1989). These data are computed from ISC/NEIC hypocentres and the Jeffreys–Bullen travel-time tables[29]. Displaying the data in this way shows that waves travelling to stations between 50° and 70° arrive systematically earlier than expected from the JB model. In the distance range of 15° and 25° the concentration of P-wave data suggests the presence of triplication branches owing to upper-mantle discontinuities unaccounted for by the JB model[30,52]. b, Northwest Pacific (NWP) P delay times computed from improved earthquake hypocentres and the iasp91 velocity model[24]. The NWP P data are evenly distributed around the axis of zero delay time: the branches between 15° and 25° are reduced because by using iasp91 we corrected for upper-mantle discontinuities, and the slightly different lower-mantle structure of iasp91 removed the systematic deviations between 25° and 90°. We remark that the mean value of the ISC P distribution is slightly closer to zero than that of the NWP P data because the ISC data are optimal with respect to ISC hypocentre locations, whereas the NWP P data are computed from hypocentres located with both P and pP data. The variance of NWP P data is 17% less than the variance of the uncorrected ISC P data. On subsequent tomographic inversion, a further variance reduction of 41% was obtained after 35 iterations (HES91).

logarithmic scale

2e02   2e10

ISC: mean = -0.03 sec σ^2 = 2.16 sec^2

a

NWP: mean = 0.11 sec σ^2 = 1.80 sec^2

b

Delay time (s)

The result of resolution tests demonstrates that our approach does provide good resolution of lower-mantle structure (HES91). Here we show only the result of a simple test. For the earthquake and station distributions shown in Fig. 1, we computed synthetic P- and pP-wave travel-time residuals through a target anomaly (8% faster than iasp91) at a depth of 975 km. We added gaussian noise to the synthetic data using typical standard errors for P and pP data (1 s and 1.5 s respectively). The (20%) contour lines of the inversion response to this target anomaly are distorted only slightly, which indicates that there is no significant 'smearing' in the dip direction of the slab.

Outside the area under study, we assume the reference Earth structure (here iasp91) and there is a danger that the images are affected by the mapping into the solution of aspherical structure outside the mantle volume under study[21,22]. The contribution to this mapping is largest from mantle regions in which the Fresnel zone of the P and pP waves decreases in size, that is, in the direct vicinity of the stations outside the study region. We therefore computed station corrections, on tomographic inver-

sion, for all stations outside the study area[36]. Where available, we used independently determined station corrections[45] as starting values for our corrections. Studies of the effects of wavefront healing (T. J. Moser and G. Nolet, manuscript in preparation) shows that lower-mantle heterogeneity has a small effect on delay-time variance, whereas systematic bias is mostly absorbed in the station correction.

From the resolution test we concluded that 'smearing' in the dip direction of the Kuril slab is not significant. Together with the observation (Fig. 5c) that low P-wave velocities are imaged below the high-velocity slab (in contrast to Fig. 5a), this leads us to conclude that the high-velocity structure below the Kuril arc does not result from the mapping of distant structure. Also, from analysis of the solution itself we can be confident that no important artefacts from heterogeneities elsewhere have been introduced into the model. Figure 6a and b shows images across the Kuril arc (for locations see Fig. 1). If aspherical structure outside the mantle volume under study contributes to the imaged high P-wave velocity in the lower mantle below the

FIG. 4 Vertical mantle sections across the Izu Bonin and Central Japan island arcs (locations are given in Fig. 1b). The seismicity of the subduction zones is shown above the tomographic images. The horizontal line depicts the 670-km discontinuity. a, Izu Boni cross-section by inversion of ISC P data. Note the bent high-velocity zone across the upper-lower mantle boundary below the Izu Bonin arc. This structure was also reported in ref. 34. b, Central Japan cross-section by inversion of ISC P data. The 'smearing' of anomalies from the bottom of the upper mantle to the surface reveals lack of resolution along P-wave ray paths to stations in Asia[26]. c, Izu Bonin cross-section by inversion of NWP P and pP data. d, Central Japan cross-section by inversion of NWP P and pP data. The tomographic images shown here and in Fig. 5 are obtained after 30 iterations of the damped LSQR inversion algorithm[36,37]. This algorithm has intrinsic damping properties that minimize artefacts in the images of mantle structure in regions with low resolution. We inverted travel-time residuals for variations in P-wave velocity relative to the one-dimensional reference velocity models shown at the right-hand side of the figures. The Earth's volume under study was parameterized by 47,850 blocks with horizontal dimensions of $1° \times 1°$ and thickness varying from 35 km for the uppermost layer to 200 km at a depth of 1,500 km (HES91).
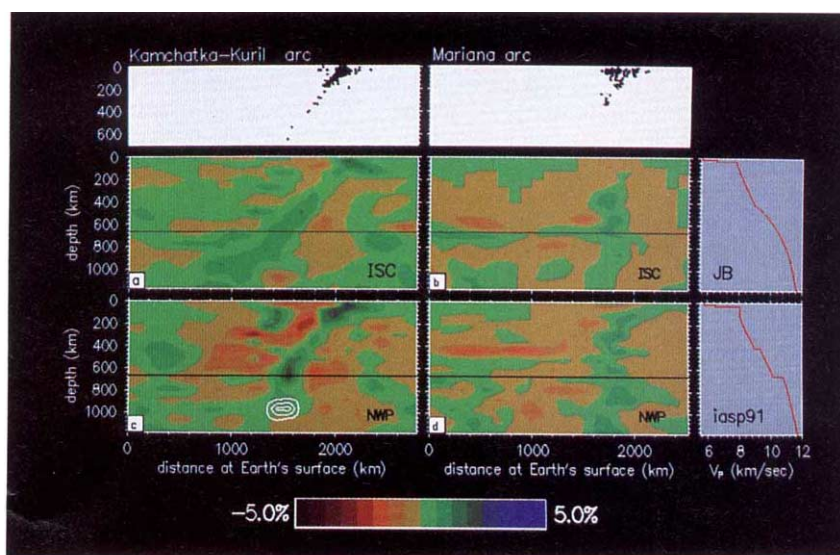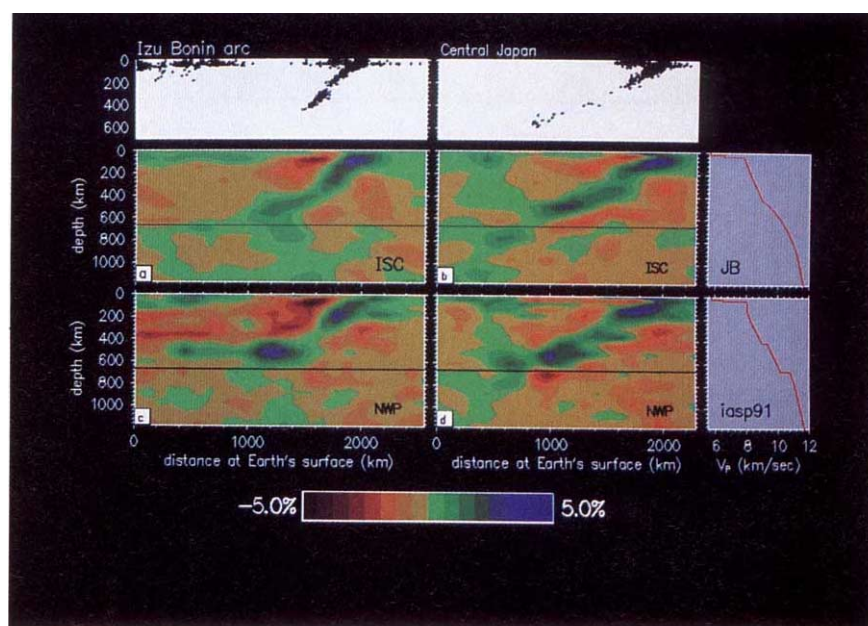

FIG. 5 Mantle sections across the Kuril and Mariana island arcs (locations given in Fig. 1). a, Kuril cross-section by inversion of ISC P data. b, Mariana cross-section by inversion of ISC P data. Note the absence of high P-wave velocities near the shallow part of the Wadati–Benioff zone. c, Kuril cross-section by inversion of NWP P and pP data d, Mariana cross-section by inversion of NWP P and pP data. In c we also show the result of a simple resolution test (see text for discussion).
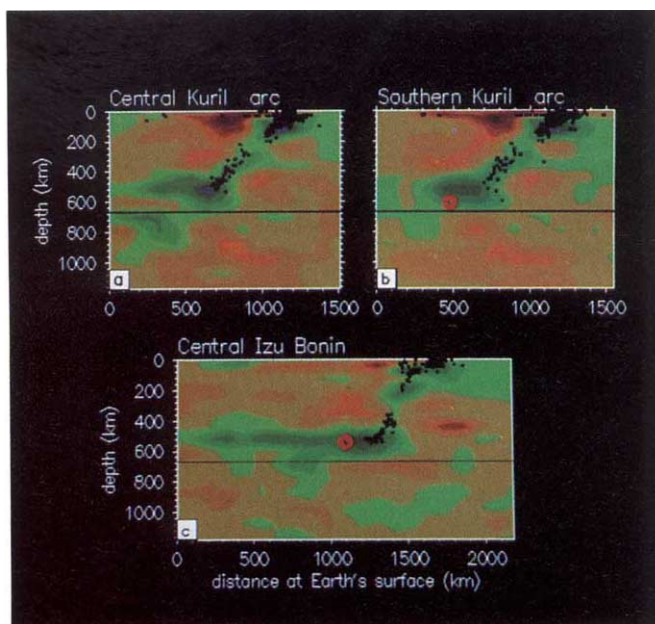
FIG. 6 Mantle cross-sections showing images of slab structure by the inversion of NWP P and pP data (locations given in Fig. 1). *a*, Central Kuril. *b*, Southern Kuril, across the island of Sakhalin. The red dot depicts the location of the earthquake that occurred on 12 May, 1990 (ref. 40). *c*, Central Izu Bonin. The red dot depicts the July 1982 earthquake[41] ($m_b = 6$).

Wadati–Benioff zone, one would expect the effect to be similar for the two images, as the sampling by seismic ray paths is about the same. This is clearly not the case.

Our images of a sub-horizontal high-velocity structure below the northern Philippine Sea Plate and the Sea of Japan are in agreement with the results of Fukao *et al.*[35], who solved simultaneously for updates of the one-dimensional reference model and for aspherical variations in seismic velocity. This indicates that our results are not artefacts of the iasp91 model. Slab deflection at the 670-km discontinuity was also suggested by Zhou and Clayton[33], but they used only a few teleseismic rays and would thus have missed steeply dipping structures in the lower mantle.

Mantle convection and subduction history

The inference that subducted slabs are deflected in the transition zone (410–670 km) below the southern Kuril, Japan and Izu Bonin arc (Figs 4c, *d* and 6b, *c*), and sink into the lower mantle below the Kuril–Kamchatka and Mariana arcs (Figs 5c, *d* and 6*a*) is in good agreement with other images obtained recently[35]. These results suggest that the boundary between upper and lower mantle acts as a strong barrier for mantle flow. The observation that (at least locally) slabs sinks into the lower mantle is, however, inconsistent with a model of strictly independent convection in the upper and lower mantle.

Seismological observations and numerical simulations of mantle flow suggest that the lower mantle is at least 10–30 times more viscous than the upper mantle[46]. Several studies of mantle convection (for a review see ref. 1) have considered variable degrees of isochemical and compositional density and viscosity contrasts between the upper and lower mantle and have shown that slab deflection and slab penetration might coexist[47–49]. A recent numerical modelling study[49] of mantle flow included compressibility and the endothermic phase change from spinel to perovskite and magnesiowustite which is associated with the seismic discontinuity at a depth of 670 km. For a shallow negative Clapeyron slope of $-2 \, \text{MPa} \, °\text{C}^{-1}$ they found intermittent mixing between the upper and lower mantle with flow structures resembling our images of subducted slab below the northwest Pacific.

Our images are consistent with a convection model that allows local mass transport across the boundary between upper and lower mantle. One should be cautious of such interpretations, however: tomographic images depict variations in seismic velocity, and from the images alone one can not unambiguously discriminate between actual mass transport across the upper–lower mantle boundary or velocity perturbations in the lower mantle resulting from thermal coupling in layered convection[50], possibly combined with a locally depressed 670 km discontinuity.

Present convection models fail to explain why subducted lithosphere deflects at the base of the upper mantle below particular island arcs, but sinks into the lower mantle below others. Results of fluid-dynamical modelling[51] suggest that subduction history plays an important role in controlling the morphology of the subducted slab near the upper–lower mantle boundary. Slab deflection at a layer with high viscosity can occur in the case of the oceanward migration of the trench owing to the roll-back of the subduction zone, whereas penetration of subducted lithosphere into a high-viscosity lower mantle is possible when the location of the trench is stable[47,51]. This provides a working model for a tentative explanation of imaged differences in slab morphology below, for instance, the Izu Bonin and Mariana island arcs. Reconstructions of the tectonic history of the Philippine Sea plate[53] indicate that, after initial onset ~45 Myr ago, the evolution of the subduction zones below the northern and southern parts of the Philippine Sea plate have been different. In the preferred kinematic model of Seno and Maruyama[53], the location of the Mariana trench has been stable, possibly triggering slab penetration, but the Izu Bonin trench migrated northwest, over hundreds of kilometres, to its present location southeast of Japan. This would be consistent with the image of a deflected slab below the Izu Bonin arc (Fig. 4c).

A detailed interpretation is beyond the scope of this paper. Nevertheless, it is clear that the integration of results of seismic imaging with information from tectonic reconstructions and fluid-dynamical modelling will ultimately lead to new understanding of the relationship between plate tectonics and mantle convection. □

1. Olson, P., Silver, P. G. & Carlson, R. W. *Nature* **344**, 209–215 (1990).
2. Jordan, T. H. & Lynn, W. S. *J. geophys. Res.* **79**, 2679–2685 (1974).
3. Jordan, T. H. *Nature* **257**, 745–750 (1975).
4. Lay, T. *Geophys. J. R. astr. Soc.* **72**, 503–516 (1983).
5. Grand, S. P. *J. geophys. Res.* **92**, 14065–14090 (1987).
6. Vidale, J. E. & Garcia-Gonzalez, D. *Geophys. Res. Lett.* **15**, 369–372 (1988).
7. van der Hilst, R. D. thesis, Univ. of Utrecht (1990).
8. Inoue, H., Fukao, Y., Tanabe, K. & Ogota, Y. *Phys. Earth planet. Inter* **59**, 294–328 (1990).

9. Brooks, D. A. et al. Tectonophysics 102, 1–16 (1984).
10. Jordan, T. H. J. geophys. Res. 43, 473–496 (1977).
11. Creager, K. C. & Jordan, T. H. J. geophys. Res. 89, 3031–3049 (1984).
12. Creager, K. C. & Jordan, T. H. J. geophys. Res. 91, 3573–3589 (1986).
13. Fischer, K. M., Jordan, T. H. & Creager, K. C. J. geophys. Res. 93, 4773–4783 (1988).
14. Silver, P. G. & Chan, W. W. J. geophys. Res. 91, 13787–13802 (1986).
15. Cormier, V. F. J. geophys. Res. 94, 3006–3024 (1989).
16. Suetsugu, D. J. Phys. Earth 37, 265–295 (1989).
17. Takei, Y. & Suetsugu, D. J. Phys. Earth 37, 225–231 (1989).
18. Dziewonski, A. M. J. geophys. Res. 89, 5929–5952 (1984).
19. Zhou, H. Geophys. Res. Lett. 15, 1425–1428 (1988).
20. Lay, T. & Young, C. J. Geophys. Res. Lett. 16, 605–608 (1989).
21. Schwartz, S. Y., Lay, T. & Grand, S. Geophys. Res. Lett. 18, 1265–1268 (1991).
22. Zhou, H., Anderson, D. L. & Clayton, R. W. J. geophys. Res. 95, 6799–6827 (1990).
23. Aki, K., Christoffersson, A. & Husebye, E. S. J. geophys. Res. 82, 277–296 (1977).
24. Kennett, B. & Engdahl, E. R. Geophys. J. 105, 429–465 (1991).
25. van der Hilst, R. D. & Engdahl, E. R. Geophys. J. 106, 169–188 (1991).
26. Spakman, W., Stein, S., van der Hilst, R. D. & Wortel, R. Geophys. Res. Lett. 16, 1097–1101 (1989).
27. Engdahl, E. R. & Billington, S. Bull. seismol. Soc. Am. 76, 77–93 (1986).
28. Engdahl, E. R. & Gubbins, D. J. geophys. Res. 92, 13855–13862 (1987).
29. Jeffreys, H. & Bullen, K. E. British Association for the Advancement of Science (London, 1967).
30. van der Hilst, R. D. & Spakman, W. Geophys. Res. Lett. 16, 1093–1096 (1989).
31. Dziewonski, A. & Anderson, D. L. J. geophys. Res. 88, 3295–3314 (1983).
32. Hirahara, K. & Mikumo, T. Phys. Earth planet Inter. 21, 109–119 (1980).
33. Zhou, H. & Clayton, R. W. J. geophys. Res. 95, 6829–6851 (1990).
34. Kamiya, S., Miyatake, T. & Hirahara, K. Geophys. Res. Lett. 15, 828–831 (1988).
35. Fukao, Y., Nenbai, M., Obayashi, M. & Inoue, H. J. geophys. Res. (submitted).
36. Spakman, W. & Nolet, G. in Mathematical Geophysics (eds Vlaar, N. J. et al.) 155–188 (Reidel, Dordrecht, 1988).
37. Paige, C. C. & Saunders, M. A. ACM Trans. Math. Soft. 8, 3–71; 195–209 (1982).
38. Nolet, G. J. comput. Phys. 61, 463–482 (1985).
39. van der Sluis, A. & van der Vorst, H. A. in Seismic Tomography (ed. Nolet, G.) 49–84 (Reidel, Dordrecht, 1987).
40. Okino, K., Ando, M., Kaneshima, S. & Hirahara, K. Geophys. Res. Lett. 16, 1059–1063 (1989).
41. Ekström, G., Dziewonski, A. & Ibañez, J. Eos 71, 1462 (1990).
42. Shearer, P. Nature 344, 121–126 (1990).
43. Anderson, D. L. Eos 71, 1473 (1990).
44. Humphreys, E. & Clayton, R. W. J. geophys. Res. 93, 1073–1085 (1988).
45. Toy, K. thesis, Univ. of California, San Diego (1990).
46. Gurnis, M. & Hager, B. Nature 335, 317–321 (1988).
47. Ringwood, A. E. & Irifune, T. Nature 331, 131–136 (1988).
48. Christensen, U. & Yuen, D. A. J. geophys. Res. 89, 4389–4402 (1984).
49. Machetel, P. & Weber, P. Nature 350, 55–57 (1991).
50. Nataf, H. C., Moreno, S. & Cardin, P. J. Phys. France 49, 1707–1714 (1989).
51. Kincaid, C. & Olson, P. J. geophys. Res. 92, 13832–13840 (1987).
52. Zielhuis, A., Spakman, W. & Nolet, G. in Digital Seismology and Modelling of the Lithosphere (eds Cassinis, R., Panza, G. & Nolet, G.) 333–340 (Plenum, London, 1988).

Assignment of G-protein subtypes to specific receptors inducing inhibition of calcium currents

C. Kleuss*, J. Hescheler†, C. Ewel*, W. Rosenthal†, G. Schultz† & B. Wittig*

* Institut für Molekularbiologie und Biochemie, and † Institut für Pharmakologie, Freie Universität Berlin, Arnimallee 22, D-W1000 Berlin 33, Germany

The inhibition of voltage-dependent Ca^{2+} channels in secretory cells by plasma membrane receptors is mediated by pertussis toxin-sensitive G proteins. Multiple forms of G proteins have been described, differing principally in their α subunits, but it has not been possible to establish which G-protein subtype mediates inhibition by a specific receptor. By intranuclear injection of antisense oligonucleotides into rat pituitary GH_3 cells, the essential role of the G_o-type G proteins in Ca^{2+}-channel inhibition is established: the subtypes G_{o1} and G_{o2} mediate inhibition through the muscarinic and somatostatin receptors, respectively.

REGULATORY GTP-binding proteins (G proteins) constitute a family of proteins involved in signal transduction across the plasma membrane[1,2]. They consist of three different subunits, α, β and γ. G proteins are classified according to their α subunits, some of which are substrates for ADP-ribosylating bacterial exotoxins, such as cholera and pertussis toxin. Sixteen G protein α subunits encoded by different genes are known, and this diversity of α subunits is increased by alternative splicing[2]. In combination with a particular α subunit, at least three types of β and four types of γ subunits contribute to an even greater variety of heterotrimeric G proteins.

G proteins transduce signals from membrane receptors to effectors like enzymes (for example, adenylyl cyclase and phospholipase C) and ion channels (such as the voltage-sensitive calcium or potassium channels). But unequivocal assignment of one G protein to a single receptor/effector system has been achieved only for G_s, the stimulatory G protein of adenylyl cyclase, and for the transducins, the retinal G proteins, which

mediate between activated photoreceptors and a cyclic GMP phosphodiesterase. As the α subunits are very similar, it is difficult to distinguish between the G-protein subtypes: recombinant G-protein subunits expressed in bacteria are not particularly active, possibly because of inadequate post-translational modification[3,4], and antibodies raised against peptides corresponding to specific regions of G-protein subtypes have little affinity for native G proteins.

Our study concerns the G_o family, which is limited to neuronal, neuroendocrine and endocrine cells[5–7], and makes use of the fact that the distinction between the α subunits of G_o subtypes is greater at nucleic acid level than in the translated protein. We have identified selective base sequences in each α subunit and designed oligodeoxynucleotides in an antisense orientation to the respective messenger RNAs for specific 'knock-out' experiments. We microinjected these oligonucleotides directly into nuclei, the presumed site of action, in controlled amounts without significantly disturbing cell-surface functions, which might happen should they be added in high concentrations to the culture medium.

Using this approach in rat pituitary GH_3 cells, we assign a function to G_o in the receptor-induced inhibition of voltage-sensitive Ca^{2+} channels and show that the subtype G_{o1} specifically mediates the action of carbachol via a muscarinic receptor and that G_{o2} transduces the signal from the somatostatin receptor. As the cytosolic Ca^{2+} concentration is regulated by Ca^{2+}-channel activity, the receptor-induced inhibition of Ca^{2+} channels by somatostatin or carbachol could be crucial for the control of secretion.

Effectiveness of microinjected antisense DNA

To check whether our procedure does suppress G-protein α subunits, we monitored cells by immunofluorescence microscopy following microinjection of antisense DNA. GH_3 cells express α subunits of $G_s(\alpha_s)$ and two forms each of α subunits of G_i and G_o (refs 8, 9). G-protein α subunits were